

# Enhanced Electrochemical Performance of Zr<sup>4+</sup> and Co<sup>3+</sup> doped LiNi<sub>0.65</sub>Mn<sub>0.35</sub>O<sub>2</sub> Cathode Material for Lithium Ion Batteries

Pengpeng Wu, Yanru Zhang \*

School of Materials Science and Engineering, Hebei University of Engineering, Handan 056038, China.

\*E-mail: [zhangyanru@hebeu.edu.cn](mailto:zhangyanru@hebeu.edu.cn)

Received: 1 March 2022 / Accepted: 12 April 2022 / Published: 7 May 2022

---

A Co-free layered cathode material has been intensively studied as the next-generation commercial Lithium-ion batteries, known for its low cost. However, the poor performance of functional capacity, rate capability, cycling performance and thermal stability is retarding their commercialization due to the lack of cobalt. Therefore, this study demonstrates the effectiveness of a Co-free layered cathode material LiNi<sub>0.65</sub>Mn<sub>0.35</sub>O<sub>2</sub> doped with a minute amount of Zr<sup>4+</sup> and Co<sup>3+</sup> for obviously improving theirs. It is shown that the cathode material S7 (designed as simultaneously doped with 3000 ppm Zr<sup>4+</sup> and 9000 ppm Co<sup>3+</sup>) exhibits the best electrochemical properties, with an initial discharge capacity as high as 191.7 mAh/g at 0.1C in the voltage range of 3.0 – 4.4V at 25°C and capacity retention of 93.6% after 50 cycles at 1 C between 3.0 and 4.5 V at 55°C, as well as excellent rate performance and thermal stability. This effective design strategy can be applied broadly to the synthesis of other Co-free cathode materials.

---

**Keywords:** Co-free, Cathode material, LiNi<sub>0.65</sub>Mn<sub>0.35</sub>O<sub>2</sub>, Lithium-ion batteries

## 1. INTRODUCTION

Nowadays, lithium-ion batteries have been extensively used in many fields, such as portable electronics, power tools, energy storage devices, and especially the electric vehicles (EVs) [1-3]. However, cost control has become the mainstream trend with the rising installed capacity in the past years [4]. As we all know, cathode materials are regarded as the most critical part in the cost control of lithium-ion batteries. Therefore, a Co-free cathode material will be gradually commercialized for EVs to take advantage of its low price.

The LiNi<sub>x</sub>Mn<sub>1-x</sub>O<sub>2</sub> of Co-free cathode materials have been paid more attention owing to its extraordinary reversible capacity, environment friendly, non-toxicity and low cost [5-7]. LiNi<sub>0.5</sub>Mn<sub>0.5</sub>O<sub>2</sub> has been recognized as the most promising product since it was introduced by Ohzuku and Makimura [8]. LiNi<sub>0.5</sub>Mn<sub>0.5</sub>O<sub>2</sub> is similar to LiCoO<sub>2</sub> which is a layered α-NaFeO<sub>2</sub> structure. In this

formulation, Ni and Mn exhibit different average valence which is +2 and +4, respectively [9]. In addition,  $\text{Ni}^{2+}$  acts as the only electrochemical element and the reaction is relied on  $\text{Ni}^{2+/4}$  re-dox couple during the charge-discharge process [10]. When  $\text{Li}^+$  is extracted from  $\text{LiNi}_{0.5}\text{Mn}_{0.5}\text{O}_2$ ,  $\text{Ni}^{2+}$  can be oxidized to  $\text{Ni}^{4+}$  to establish that fact  $\text{Mn}^{4+}$  takes no participation in this reaction [11]. Just as we known,  $\text{Mn}^{4+}$  only maintains the structural stability which constitutes one of the most stable ions during electrochemical operation.

Unfortunately, it deems that there are likewise some problems for the  $\text{LiNi}_x\text{Mn}_{1-x}\text{O}_2$  cathode material. On the one hand,  $\text{Ni}^{4+}$  is full of higher activeness reacting with the electrolyte, which could bring to a relentless capacity attenuation, bad cycling performance and poor rate performance [12-14]. On the other hand, it can easily lead to Li/Ni disorder because of the striking ionic radii similarity between  $\text{Li}^+$  (0.076 nm) and  $\text{Ni}^{2+}$  (0.069 nm). At this point, part of  $\text{Ni}^{2+}$  in the transition metal layer will migrate to Li layer, occupying the Li sites. This phenomenon will impede the  $\text{Li}^+$  transferring process, leading to aggravation of side reactions at the interface. It could further deliver the capacity loss and poor rate performance [15-17]. To date, Li/Ni cation mixing, as always, is paid more attention by researchers.

Subsequently, cathode materials with diverse ratios of nickel and manganese have been developed, for instance,  $\text{LiNi}_{2/3}\text{Mn}_{1/3}\text{O}_2$  [18],  $\text{LiNi}_{0.7}\text{Mn}_{0.3}\text{O}_2$  [19-20] and so on. A large number of scientific researchers have come up with some ways to improve electrochemical performance of the cathode materials, mainly by doping and coating. It is well known for all that doping with a few transition metal ions (e.g.  $\text{Mg}^{2+}$ ,  $\text{Al}^{3+}$ ,  $\text{Ti}^{3+}$ ,  $\text{Zr}^{4+}$ ,  $\text{Co}^{3+}$ ) can slow down the voltage decline, volume change and improve  $\text{Li}^+$  diffusion rate [21-23]. Not only can coating protect active cathode material from the electrolyte to reduce the side reactions, but also enhance the electronic conductivity or ionic conductivity. For example, nano-scale alumina has been commonly used in industrial mass production [24]. Moreover, some literature suggests that cation disorder tends to decrease with the rising of calcination temperature around 900 – 1000°C.

In the past three years, the conventional single crystal cathode material of  $\text{LiNi}_{0.6}\text{Co}_{0.2}\text{Mn}_{0.2}\text{O}_2$  has been commercialized, followed by  $\text{LiNi}_{0.65}\text{Co}_{0.15}\text{Mn}_{0.2}\text{O}_2$  and  $\text{LiNi}_{0.65}\text{Co}_{0.07}\text{Mn}_{0.28}\text{O}_2$  with the decreasing cobalt content. It can be speculated that cobalt-free materials while the Ni content is 65% will be put into commercial applications.

In this study, we synthesized the  $\text{LiNi}_{0.65}\text{Mn}_{0.35}\text{O}_2$  doped with different amount of  $\text{Co}^{3+}$  and  $\text{Zr}^{4+}$  cathode materials by a solid-state reaction. All of the cathode materials were investigated by means of X-ray diffraction (XRD), scanning electron micros-copy (SEM), inductively coupled plasma (ICP), differential scanning calorimetry (DSC) and Beckman particle size analyzer to explain the structure transition and residual lithium content ( $\text{Li}_2\text{CO}_3$  and  $\text{LiOH}$ ) on the surface.

## 2. EXPERIMENTAL

### 2.1 Preparation

The cathode materials were obtained by a solid-state method. The first step, hydroxide precursor  $\text{Ni}_{0.65}\text{Mn}_{0.35}(\text{OH})_2$  was mixed with a stoichiometric amount of  $\text{LiOH}\cdot\text{H}_2\text{O}$  (10 wt% in excess)

and additional agent ( $\text{Co(OH)}_2$  and  $\text{ZrO}_2$ ) by mechanical mixing. The uniformity of the mixture can be evaluated by the ICP results of three different positions. The second, obtained mixture was heated at  $600^\circ\text{C}$  for 3h and  $940^\circ\text{C}$  for 12h and then slowly cool down to room temperature under an  $\text{O}_2$  atmosphere in the furnace. Finally, synthetic cathode materials were coated by nano-scale alumina. The obtained samples named S1-S8 are given in Table 1.

## 2.2 Characterization

The particle size distribution of the cathode materials was measured by a Beckman particle size analyzer.

The powder XRD data of the samples was collected by RigakuRint 2200 diffractometer with  $2\theta$  in the range of  $10^\circ - 80^\circ$  and a step size of  $0.02^\circ$ , holding at each step for 0.24s.

The morphology of the samples was characterized by scanning electron microscopy (SEM, EVO MA 15). Thermal stability studies were performed using a differential scanning calorimetry (DSC, NETZSCH-STA-449C).

Inductive coupled plasma-atomic emission spectrometry (ICP-AES, IRIS INTREPID II) was conducted on the product to identify the uniformity of element distribution. Free  $\text{Li}^+$  was analyzed by automatic potentiometric titrator.

## 2.3 Electrochemical measurements

Electrochemical tests were conducted using a CR2032-type coin cell. The sample were mixed with a conducting agent (super P carbon black) and polyvinylidene fluoride (PVDF) binder in a weight ratio of 90:4:6 in NMP (N-methyl-2-pyrrolidone) to form a slurry, which was spread on onto an aluminum foil current collector dried in the vacuum oven at  $120^\circ\text{C}$  for 2h. Disks of electrode film with a diameter of 14 mm were punched. The cells were assembled in an argon-filled glove box ( $\text{O}_2 < 1$  ppm and  $\text{H}_2\text{O} < 1$  ppm) with metallic lithium foil as the counter electrode, Celgard 2500 film as the separator and 1 mol/L  $\text{LiPF}_6$  in a mixture of ethylene carbonate (EC) / dimethyl carbonate (DMC) (EC/DMC, 1:1 in volume) as the electrolyte. The galvanostatic charge-discharge testing was performed by a LAND battery testing system with different C rates between 3.0 – 4.4V at  $25^\circ\text{C}$ . Cycling performance of the cells was also investigated by galvanostatic methods in the potential range of 3.0 – 4.5 V at  $55^\circ\text{C}$ .

## 3. RESULTS AND DISCUSSION

As Table 1 show, there is a certain gap between the testing result and theoretical content because of the elements volatilization at high temperatures and a margin of detecting tolerance error.

**Table 1.** The doping content of synthesized cathode materials as measured by ICP-MS

Sample	Target Co <sup>3+</sup> doping /ppm	Target Zr <sup>4+</sup> doping /ppm	Measured Co <sup>3+</sup> doping /ppm	Measured Zr <sup>4+</sup> doping /ppm
S1	0	0	0	0
S2	0	1000	0	896
S3	0	3000	0	2378
S4	0	5000	0	4126
S5	3000	3000	2319	2346
S6	6000	3000	5109	2443
S7	9000	3000	8315	2217
S8	12000	3000	11367	2365

Fig. 1. shows Rietveld refinement results of XRD patterns for the sake of identifying the crystal structure of the synthesized powders. The XRD patterns belong to the  $\alpha$ -NaFeO<sub>2</sub> structure (space group R $\bar{3}m$ ) without remarkable secondary phase because of the least doping amount [11]. There is apparent splitting between the (006) / (102) and (108) / (110) peaks in the XRD magnification pattern indicating an ideal layered structure. Generally, it is considered that ratio of c/a can be also indexed on the layered structure. For larger c/a ratios, it is a better layered structure on account of the smaller Li/Ni cation mixing. As showed in Table 2, the only more doping amount of Zr<sup>4+</sup>, the larger c/a value, showing the optimal doping amount is 3000 ppm. It is observed that growing cobalt content can improve the layered structure indicating the optimal doping level of Co<sup>3+</sup> is 9000 ppm while double elements doped. Integrated intensity ratios of I<sub>003</sub>/I<sub>104</sub> (R) could have something to do with the degree of cationic disorder. In general, it has made it possible that all obtained cathode materials show the relatively weaker cation mixing with the R value more than 1.2. As can be seen from Table 2, the relative intensity of (I<sub>006</sub>+I<sub>102</sub>)/I<sub>101</sub> which can represent the order of Ni atoms to some degree has a downward trend with the amount of doping increasing. The smaller the value, the higher the orderliness of Ni atoms.

**Table 2.** Cell parameters for all cathode materials

Sample	a	c	c/a	I <sub>003</sub> /I <sub>104</sub>	(I <sub>006</sub> +I <sub>102</sub> )/I <sub>101</sub>
S1	2.8699	14.2152	4.953	1.212	0.461
S2	2.8689	14.2154	4.955	1.205	0.458
S3	2.8681	14.2165	4.957	1.289	0.449
S4	2.8682	14.2162	4.956	1.259	0.447
S5	2.8674	14.2164	4.958	1.251	0.439
S6	2.8668	14.2161	4.959	1.315	0.436
S7	2.8659	14.2157	4.960	1.312	0.431
S8	2.8664	14.2156	4.959	1.319	0.433

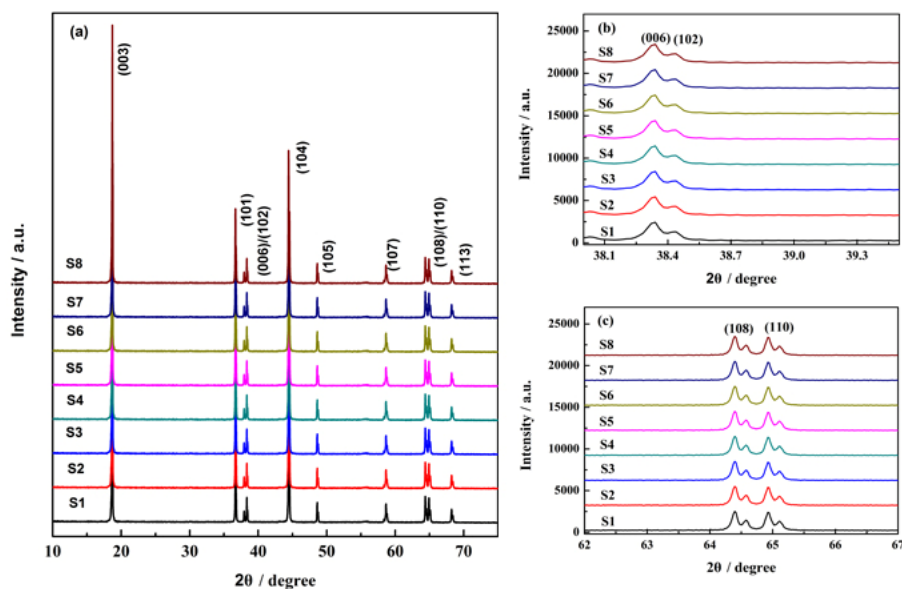


**Figure 1.** (a) XRD patterns of the prepared cathode materials (b) The magnification of (006) and (102) peaks for all materials (c) The magnification of (108) and (110) peaks for all materials

The morphology of the prepared powders is given in SEM. As providing in Fig. 2. , it can be seen that all cathode materials form morphology of single crystals. The primary material particle size is larger than other samples because of the agglomerated. There are still some agglomerates after  $Zr^{4+}$  doping. When  $Co^{3+}$  doping content rising, agglomerates have become less and less which could attribute to the higher activity of  $Co^{3+}$  that contributes to the improvement of crystallization performance. Particle size of D50 obtained from Table S1 and Figure S1 (supporting information) is consistent with SEM.

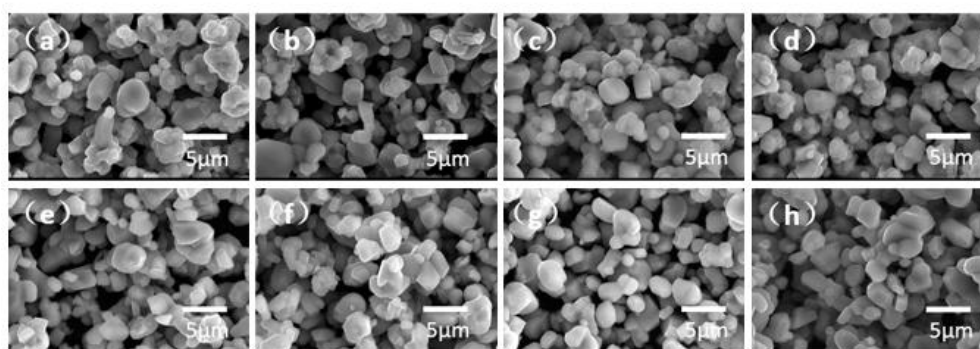


**Figure 2.** SEM images of the cathode materials (a) S1 (b) S2 (c) S3 (d) S4 (e) S5 (f) S6 (g) S7 (h) S8

Moreover, information of  $< 1\mu m$  and  $< 2\mu m$  should be paid more attention because the ultrafine powder could exert influence on the uniformity of homogenate and coating process. Excessive ultrafine powder enlarging the contact area with electrolyte could also aggravate the capacity degradation during battery cycling.

Satisfactory detection results for free  $\text{Li}^+$  are listed in Table S2 (supporting information). It is well-known that free  $\text{Li}^+$  could react with the electrolyte to produce carbon dioxide causing the swelling battery, especially  $\text{Li}_2\text{CO}_3$ . After that, the battery will be affected. As can be observed in the Table S2 (supporting information), the value of  $\text{Li}_2\text{CO}_3$  drop gradually with the increasing  $\text{Co}^{3+}$ , simultaneously reduced agglomerates and improved the crystallinity. Therefore, it is necessary for cathode materials to control residual alkali in industrial production.

The thermal decomposition behavior of nickel manganese double hydroxide and the precursor mixed with  $\text{LiOH}\cdot\text{H}_2\text{O}$  is simultaneously investigated by thermal analysis technique. Fig. 3a. shows the TG and DSC curves of the precursor between 25 and  $1000^\circ\text{C}$  in  $\text{O}_2$  atmosphere. The weight decline slightly below  $150^\circ\text{C}$  can be attributed to the removal of adsorbed water, responding an endothermic peak at  $106^\circ\text{C}$ . The next mass loss between  $150^\circ\text{C}$  and  $400^\circ\text{C}$  is caused by the decomposition of composite oxalates, corresponding to the endothermic peak at  $473^\circ\text{C}$ . Fig. 3b. shows the TGA curve of the mixture in the range of  $25 - 1000^\circ\text{C}$  in  $\text{O}_2$  atmosphere. Rapid weight loss below  $110^\circ\text{C}$  can be mainly ascribed to the loss of crystal water of  $\text{LiOH}\cdot\text{H}_2\text{O}$ , corresponding to the endothermic peak at  $105^\circ\text{C}$ . In the region from  $110$  to  $270^\circ\text{C}$ , the continuous tardily mass loss could be mostly related to the removal of absorbed water in the precursor, related endothermic peak at  $224^\circ\text{C}$ . As the temperature increases from  $270$  to  $400^\circ\text{C}$ , the next tremendous weight loss can be interpreted as the decomposition of nickel manganese double hydroxide precursor and a part of  $\text{LiOH}$ , in relation to endothermic peak at  $289^\circ\text{C}$ . With the temperature rising between  $400$  and  $800^\circ\text{C}$ , a slowly decreasing curve in mass is observed, supporting an evidence that the remaining precursor and  $\text{LiOH}$  are decomposed into corresponding oxides, taking a small exothermic peak at  $465^\circ\text{C}$ . The mass drops slower and slower above  $800^\circ\text{C}$  on account of the volatilization of lithium and the release of hydrogen, produced by the transformation into the target materials of two oxide reactants, displaying an imperceptible exothermic peak at  $962^\circ\text{C}$ . Subsequently, the higher temperature leads to the material decomposition. Thus, on the premise of ensuring the size and integrity of the single crystal, it is very necessary to raise sintering temperature as much as possible to secure a lower cation mixing.

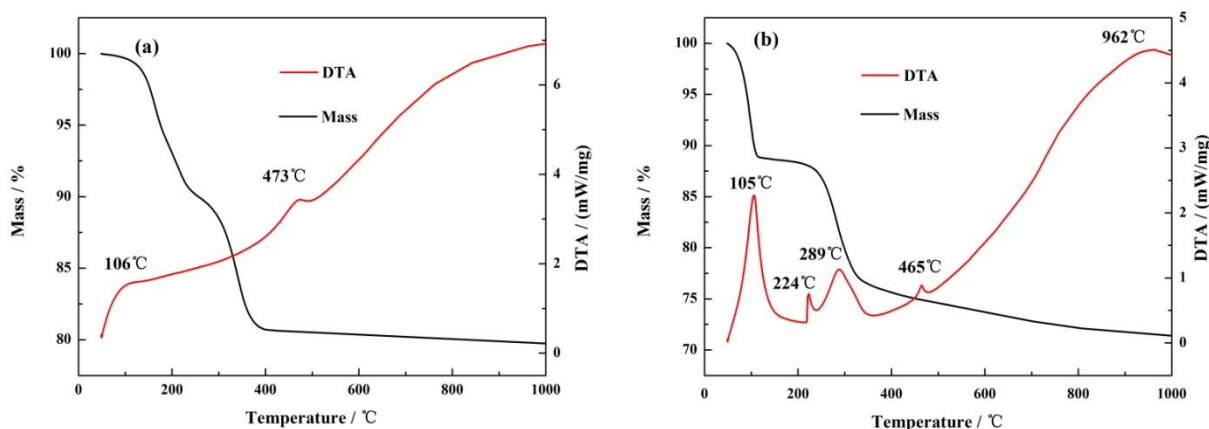


**Figure 3.** (a) DSC curves for  $\text{Ni}_{0.65}\text{Mn}_{0.35}(\text{OH})_2$  (b) DSC curves for a mixture of  $\text{Ni}_{0.65}\text{Mn}_{0.35}(\text{OH})_2$  and  $\text{LiOH}\cdot\text{H}_2\text{O}$

For the purpose of the optimal electrical performance, some comparison previously reported has been made to apply to preparation of cathode material. As shown in Table 3,  $\text{LiNi}_{0.5}\text{Mn}_{0.5}\text{O}_2$ ,  $\text{LiNi}_{0.475}\text{Al}_{0.05}\text{Mn}_{0.475}\text{O}_2$  and  $\text{LiNi}_{0.5}\text{Mn}_{0.45}\text{Ti}_{0.05}\text{O}_2$  attain the initial discharge capacity of 155 mAh/g, 175 mAh/g and 175 mAh/g, especially. It provides the fact that a certain amount of doping is beneficial to the capacity of cathode materials, corresponding to enhancement of structural integrity by element doping [22]. It can be concluded that the higher the nickel content, and the higher the capacity while the cobalt is constant. For instance,  $\text{LiNi}_{0.5}\text{Mn}_{0.5}\text{O}_2$ ,  $\text{LiNi}_{2/3}\text{Mn}_{1/3}\text{O}_2$  and  $\text{LiNi}_{0.7}\text{Mn}_{0.3}\text{O}_2$  exert the initial discharge capacity of 155 mAh/g, 172 mAh/g and 179.7 mAh/g [18, 20, 22]. In addition, the same composition may exhibit different capacities due to the difference of calcination temperature and calcining atmosphere. As for  $\text{LiNi}_{0.7}\text{Mn}_{0.3}\text{O}_2$ , manganese is substituted by 15% cobalt which will inevitably lead to the improvement of capacity by reducing Li/Ni anti-sites and maintaining structure stability [20, 23, 28]. Zr doping mitigates the degree of cation mixing, decreases the structural transformation, and facilitates  $\text{Li}^+$  diffusion bringing about enhanced coulombic efficiency, cyclic performance and rate capability although capacity degrades with excessive Zr doping [27].

**Table 3.** Comparison of previously reported work on the cathode materials

Cathode materials	Coulombic efficiency (%)	Cpacity (mAh/g)	ref
$\text{LiNi}_{2/3}\text{Mn}_{1/3}\text{O}_2$	74.80	172.0	[18]
$\text{LiNi}_{0.7}\text{Mn}_{0.3}\text{O}_2$	71.04	179.7	[20]
$\text{LiNi}_{0.5}\text{Mn}_{0.5}\text{O}_2$	73.00	155.0	[22]
$\text{LiNi}_{0.475}\text{Al}_{0.05}\text{Mn}_{0.475}\text{O}_2$	88.00	175.0	[22]
$\text{LiNi}_{0.5}\text{Mn}_{0.45}\text{Ti}_{0.05}\text{O}_2$	78.00	175.0	[22]
$\text{LiNi}_{0.7}\text{Mn}_{0.3}\text{O}_2$	89.40	176.0	[23]
$\text{LiNi}_{0.6}\text{Co}_{0.2}\text{Mn}_{0.2}\text{O}_2$	97.20	188.6	[27]
$\text{LiNi}_{0.59}\text{Zr}_{0.01}\text{Co}_{0.2}\text{Mn}_{0.2}\text{O}_2$	98.70	185.2	[27]
$\text{LiNi}_{0.7}\text{Co}_{0.15}\text{Mn}_{0.15}\text{O}_2$	/	189.0	[28]
S7 (this study)	88.20	191.7	/

To study the electrochemical properties of obtained materials, the assembled cells were initially subjected to preconditioning cycles at 0.1C rate at 25°C operated in the potential range of 3.0 – 4.4 V versus Li/Li<sup>+</sup>. The corresponding initial charge-discharge curves and coulombic efficiency for each cell are provided in Fig. 4a-c. It is easily observed that the initial discharge capacity of the samples (S2-S4) has nothing to do with Zr<sup>4+</sup> content. In contrast, samples (S5-S8) simultaneously doped with Co<sup>3+</sup> exhibit the higher initial discharge capacity and the sample S7 attains the highest initial discharge capacity of 191.7 mAh/g, better than other comparison materials previously reported (Table 3). Initial coulombic efficiency is steadily increased along with Zr<sup>4+</sup> and Co<sup>3+</sup>, while excessive doping of sample S8 begin to fall. These results reveal that the initial discharge capacity and coulombic efficiency is related not only to an amount of Zr<sup>4+</sup> and Co<sup>3+</sup> but also to the morphology of the material. As observed in Fig. 2a, the aggregated made up of smaller primary particles improve the capacity and coulombic efficiency to a certain extent. Besides, more attention should be paid to the coulombic efficiency while the excessively lower coulombic efficiency could reduce the capacity and life of the battery.

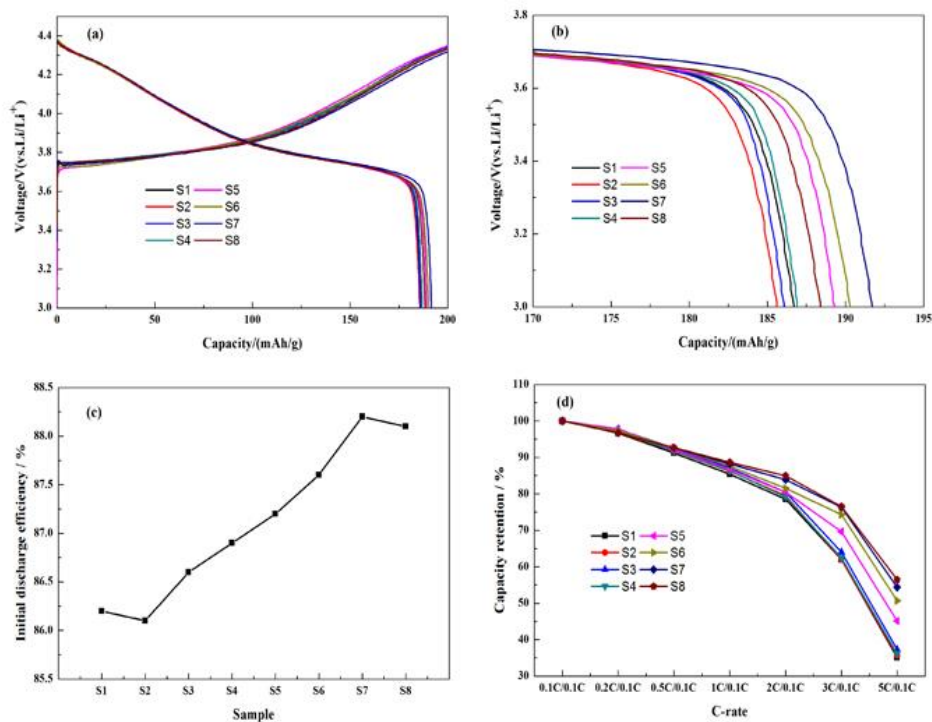


**Figure 4.** The electrochemical properties of a lithium-ion cell assembled with all prepared cathode materials (a) Initial charge and discharge curves at 0.1 C rate (b) The magnification of the 0.1 C discharge curves (c) Initial coulombic efficiency (d) Capacity retention at different rates

The cells after preconditioning cycle at 0.1C deliver a charge-discharge test at C-rates of 0.2C, 0.5C, 1C, 2C, 3C and 5C. The corresponding capacity is given in Table S3 (supporting information). The rate performance of the different cells is compared by the capacity ratio of C-rates / 0.1C called capacity retention. As showing in Fig. 4d. , it is clearly observed that the primary sample S1 delivers a discharge capacity of 65.6 mAh/g at 5C, which exerts the poorest rate capability because the capacity retention is 35.1%. After doped, the discharge capacity of modified samples S2-S8 is 66.1 mAh/g, 69.4 mAh/g, 67.6 mAh/g, 85.4 mAh/g, 96.5 mAh/g, 104.3 mAh/g and 106.4 mAh/g, respectively. Correspondingly, its capacity retention is 35.6%, 37.3%, 36.2%, 45.1%, 50.7%, 54.4%, 56.5%, which is higher than pristine sample S1. Therefore, it can conclude that Zr<sup>4+</sup> has a little effect on the improvement of rate performance while this phenomenon has been greatly promoted by Co<sup>3+</sup>, especially at 5 C. As we all known, both stable Zr<sup>4+</sup> supporting Li<sup>+</sup> layer and activated Co<sup>3+</sup> could promote Li<sup>+</sup> transmission.

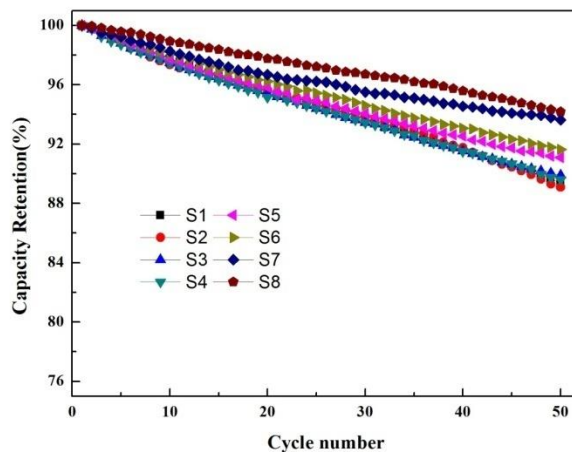


**Figure 5.** Cycling performance at 1C rate of the samples

To demonstrate the cycling stability, we cycled the cells between 3.0 – 4.5V at 55°C at a 1C rate to accelerate capacity fading. Cycle performance curves are illustrated in Fig. 5. The pristine product S1 shows an initial discharge capacity of 196.3 mAh/g at 1C and capacity retention is 89.3% after 50 cycles. However, the initial discharge capacity of modified samples S2-S8 is 197.4 mAh/g, 199.8 mAh/g, 200.1 mAh/g, 200.8 mAh/g, 201.8 mAh/g, 202.6 mAh/g, 202.2 mAh/g, and capacity retention of 89.1%, 89.8%, 89.6%, 91.1%, 91.6%, 93.6%, 94.2%, respectively. Obviously, it can be seen the cycling stability is superior to  $\text{LiNi}_{0.45}\text{Ba}_{0.05}\text{Mn}_{0.5}\text{O}_2$  reporting the 50th cycle discharge capacity at 151.4mAh/g with a capacity retention of 87.31% [9]. Similarly, it can be apparently seen that the modified materials exhibit the higher discharge capacity and better cycle stability. This is accountable for two reasons. On the one hand, high-valence  $\text{Zr}^{4+}$  could inhibit the conversion of  $\text{Ni}^{2+}$  to  $\text{Ni}^{4+}$  which could catalyze the oxidative decomposition of the electrolyte to accelerate fading. Moreover,  $\text{Zr}^{4+}$  will migrate to the surface of the electrode during the cycle to form a protective layer rendered the material more resistant to HF attack. On the other hand,  $\text{Co}^{3+}$  can reduce structural phase transitions during  $\text{Li}^+$  transmission and inhibit the migration of  $\text{Ni}^{2+}$  to the  $\text{Li}^+$  layer lowering the cation disorder. In addition,  $\text{Co}^{3+}$  also decreases the polarization and enhances structural stability during cycling.

It is well-known that battery safety has a great relationship with the thermal stability of the cathode materials in the charged state. According to the results of electrochemical performance, thermal stability of samples was selectively characterized by DSC test. Fig. 6. shows DSC thermograms of the pristine and the most optimized sample (S7), which are charged to 4.4V at 0.1C after battery activation keeping half of the delithiation. The pristine electrode (S1) has a main exothermic peak with a reaction heat of 93.3 J/g at 257°C. In contrast, the main exothermic peak of the most optimized electrode (S7) is shifted to the higher temperature of 286°C while the output of heat detail is remarkably decreased to 45.2 J/g. It is observed that doping of  $\text{Zr}^{4+}$  and  $\text{Co}^{3+}$  can improve the stability of the material. This phenomenon was interpreted that the stable  $\text{Zr}^{4+}$  can support  $\text{Li}^+$  layer

which results in the easier embedment and de-intercalation of  $\text{Li}^+$ , and  $\text{Co}^{3+}$  could reduce the structural phase transition during the charging and discharging process.

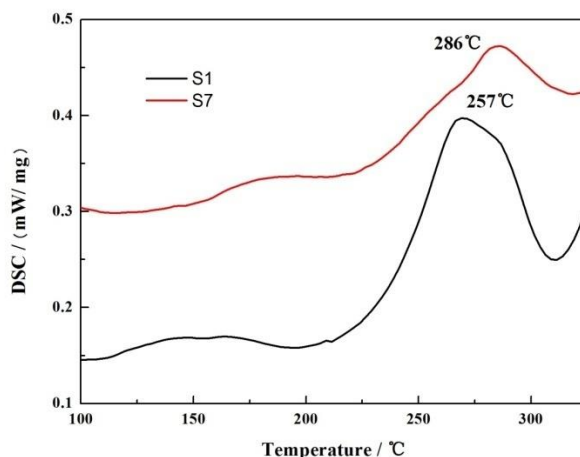


**Figure 6.** DSC thermograms of the cathode materials charged to 4.4V at 0.1C after battery activation keeping half of the delithiation

#### 4. CONCLUSION

In this study, a series of layered  $\text{LiNi}_{0.65}\text{Mn}_{0.35}\text{O}_2$  cathode materials have been successfully synthesized via a solid-state method, which were systematically explored for the ideal doping amount of  $\text{Zr}^{4+}$  and  $\text{Co}^{3+}$ . The sample S7 (simultaneously doped with 3000 ppm  $\text{Zr}^{4+}$  and 9000 ppm  $\text{Co}^{3+}$ ) exhibits the best electrochemical properties, with an initial discharge capacity as high as 191.7 mAh/g at 0.1C in the voltage range of 3.0 – 4.4V at 25°C and capacity retention of 93.6% after 50 cycles at 1 C between 3.0 and 4.5 V at 55°C, as well as excellent rate performance and thermal stability. This phenomenon can be explained that substitution of  $\text{Zr}^{4+}$  and  $\text{Co}^{3+}$  could not only enhance the  $\text{Li}^+$  transmission, but also could decrease the structural phase transition during the charge-discharge process. The concept presented in this work will provide helpful guides to the synthesis of other cathode materials with acceptable discharge capacity, cycling property and excellent rate performance.

#### ACKNOWLEDGMENTS

This work was supported by Hebei University of Engineering, China. (No. SJ2101003014).

## SUPPORTING INFORMATION

**Table S1.** Particle size distribution data for all cathode materials

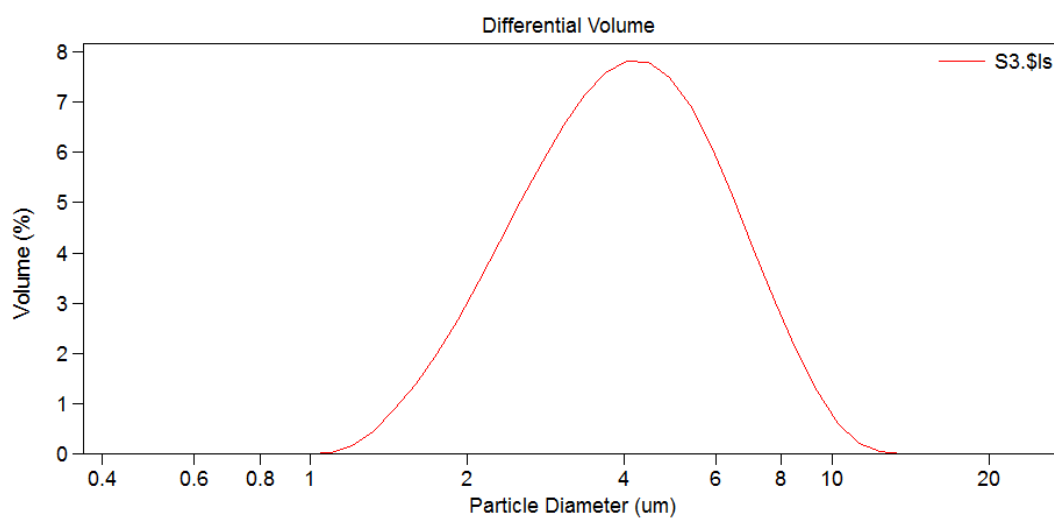
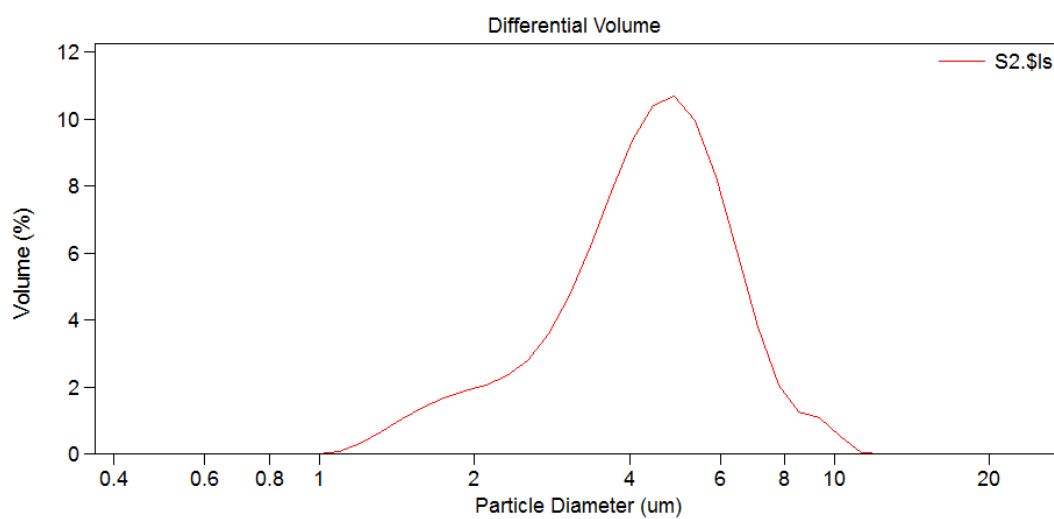
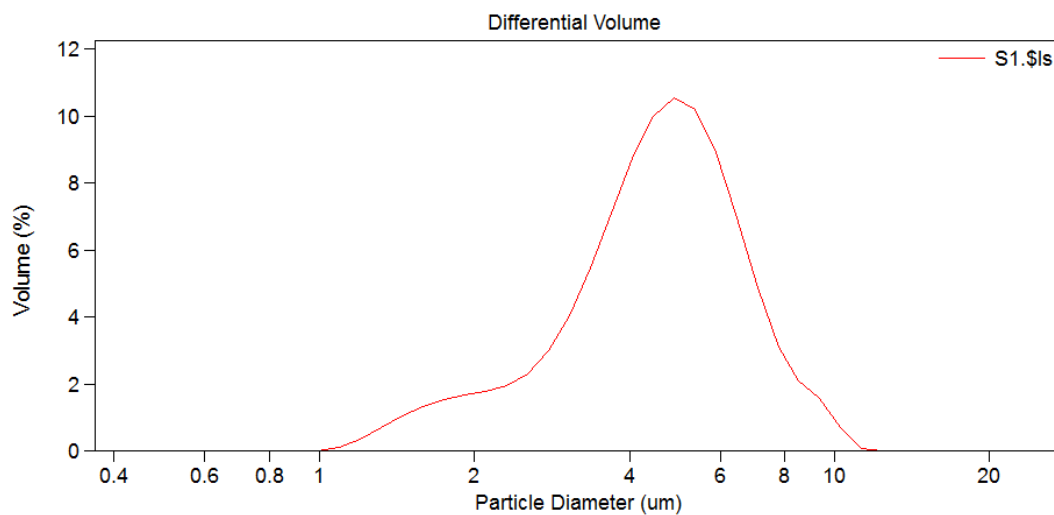
Sample	<1 $\mu$ m	<2 $\mu$ m	D50
S1	0	6.60	4.61
S2	0	6.96	4.40
S3	0	7.46	3.99
S4	0.18	12.3	3.65
S5	0.06	10.4	3.73
S6	0	6.43	4.44
S7	0.71	14.7	3.56
S8	0	5.25	4.69

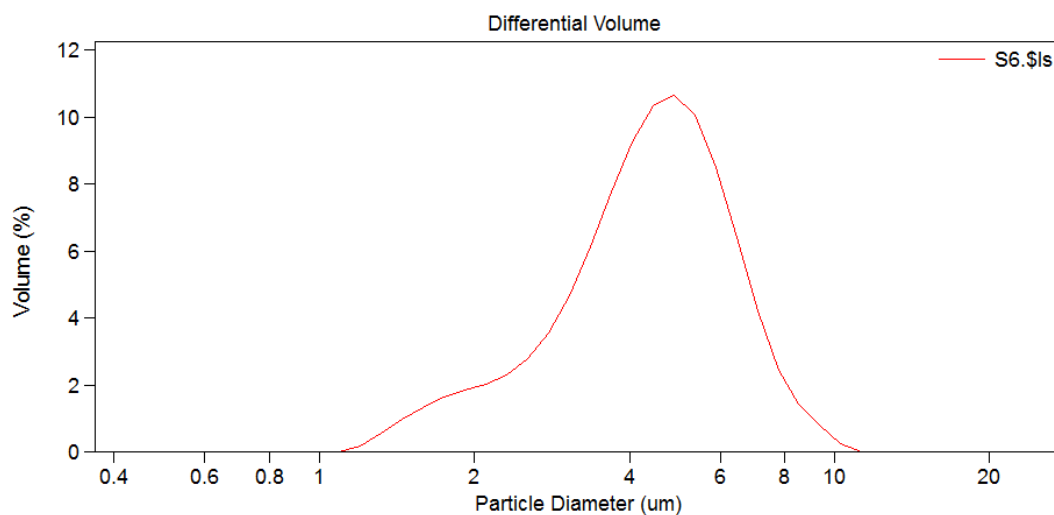
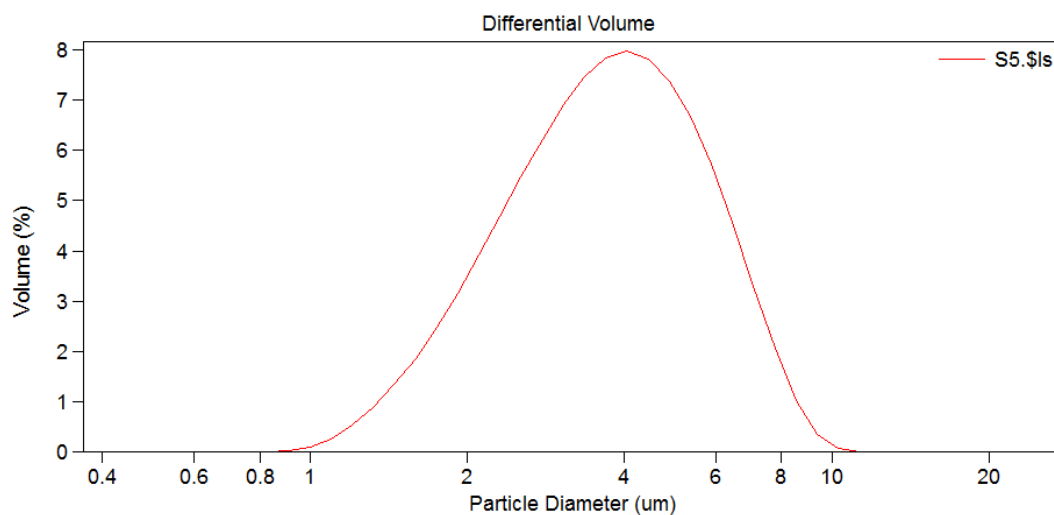
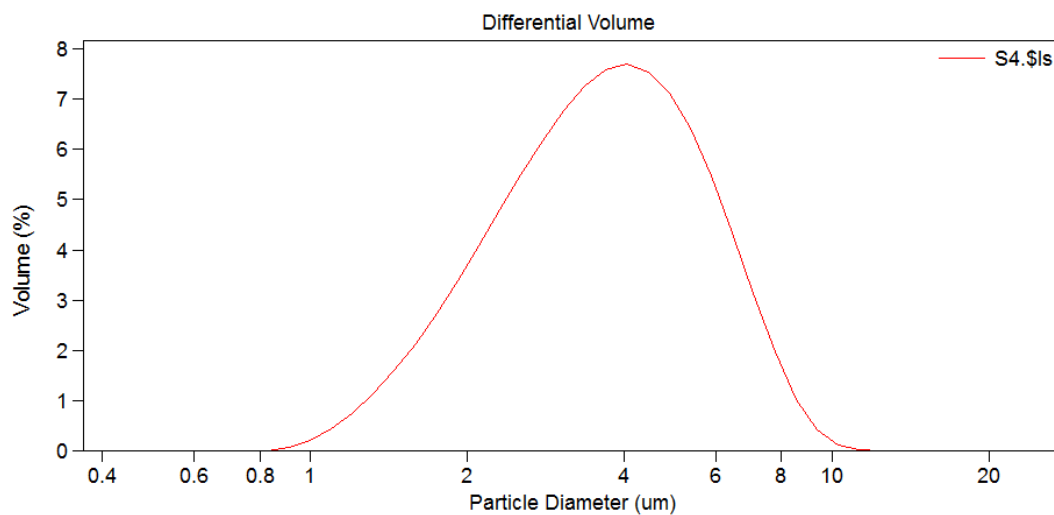
**Table S2** Free Li<sup>+</sup> for all cathode materials

Sample	Free Li <sup>+</sup> / ppm	Li <sub>2</sub> CO <sub>3</sub> / ppm	LiOH / ppm
S1	3252	1773	961
S2	2995	1751	808
S3	2632	1712	598
S4	3222	1907	852
S5	3117	1308	1175
S6	2399	751	1070
S7	2113	728	898
S8	2162	841	858

**Table S3** Capacity at different rates for all cathode materials

Sample	0.1C/m Ah/g	0.2C/mA h/g	0.5C/mA h/g	1C/mA h/g	2C/mA h/g	3C/mA h/g	5C/mA h/g
S1	186.7	180.5	170.3	159.5	146.6	115.7	65.6
S2	185.6	180.0	170.2	160.0	147.5	115.1	66.1
S3	186.1	181.8	172.2	162.1	149.7	119.1	69.4
S4	186.9	181.6	171.6	161.3	148.0	116.8	67.6
S5	189.3	185.1	174.5	164.1	152.3	131.9	85.4
S6	190.3	185.3	176.3	166.7	155.1	141.4	96.5
S7	191.7	185.5	177.6	169.1	160.8	146.3	104.3
S8	188.4	182.2	174.7	167.1	160.1	144.1	106.4





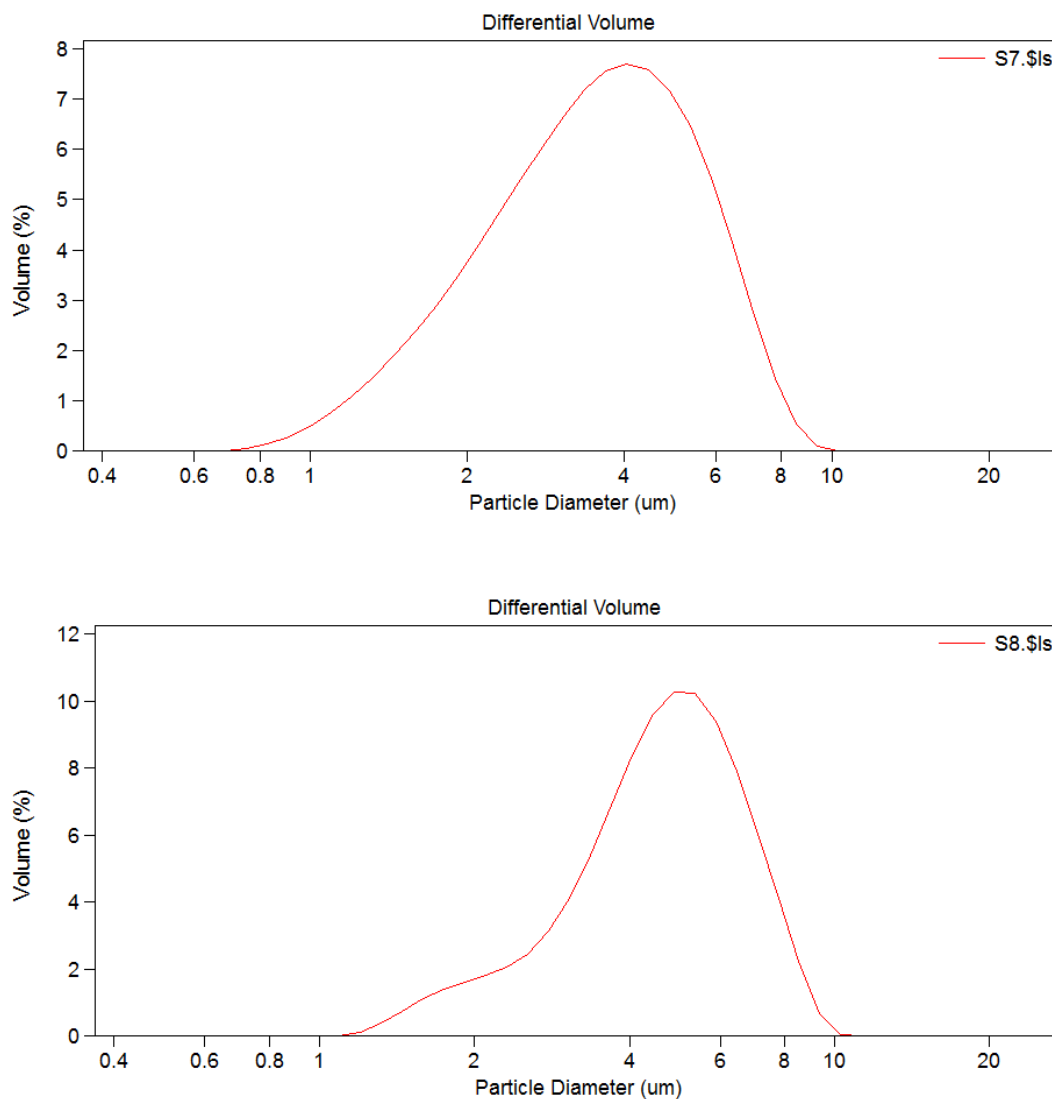


**Fig. S1.** Particle size distribution diagram for all cathode materials

## References

1. J. B. Goodenough and Y. Kim, *Chem. Mater.*, 22 (2010) 587.
2. S. W. Kim, J. H. Yun, B. Son, Y. G. Lee, K. M. Kim, Y. M. Lee and K. Y. Cho, *Adv. Mater.*, 26 (2014) 2977.
3. J. M. Tarascon and M. Armand, *Nature*, 414 (2001) 359.
4. Y. J. Gu, Y. B. Chen, H. Q. Liu, Y. M. Wang, C. L. Wang and H. K. Wu, *J. Alloys Compd.*, 509 (2011) 7915.
5. Z. Lu, D. D. Macneil and J. R. Dahn, *Electrochem. Solid-State Lett.*, 4 (2001) A191.
6. Z. Lu, L. Y. Beaulieu, R. A. Donaberger, C. L. Thomas and J. R. Dahn, *J. Electrochem. Soc.*, 149 (2002) A778.
7. Y. Liu, F. Cao, B. Chen, X. Zhao, S. L. Suib, H. L. Chan and J. Yuan, *J. Power Sources*, 206 (2012) 230.
8. T. Ohzuku and Y. Makimura, *Chem. Lett.*, 30 (2001) 744.
9. Z. Liu, H. Zheng, L. Tan, S. Yuan and H. Yin, *Energy Technol.*, 6 (2018) 1302.
10. F. L. Liu, S. Zhang, C. Deng, Q. Wu, M. Zhang, F. L. Meng, H. Gao and Y. H. Sun, *J. Electrochem.*

- Soc., 159 (2012) A1591.
11. S. T. Myung, S. Komaba, N. Hirosaki, K. Hosoya and N. Kumagai, *J. Power Sources*, 146 (2005) 645.
  12. E. Zhao, M. Chen, D. Chen, X. Xiao and Z. Hu, *ACS Appl. Mater. Interfaces*, 7 (2015) 27096.
  13. G. Jia, S. Liu, G. Yang, F. Li, K. Wu, Z. He and X. Shangguan, *Ionics*, 24 (2018) 3705.
  14. M. Labrini, I. Saadoune, F. Scheiba, A. Almaggoussi, J. Elhaskouri, P. Amoros, H. Ehrenberg and J. Brötz, *Electrochim. Acta*, 111 (2013) 567.
  15. X. Zhang, W. J. Jiang, A. Mauger, Qilu, F. Gendron and C. M. Julien, *J. Power Sources*, 195 (2010) 1292.
  16. K. Kang, Y.S. Meng, J. Breger, C. P. Grey and G. Ceder, *Cheminform.*, 311 (2006) 977.
  17. T. Gao, G. Yang, B. Yang and Y. Dai, *J. Alloys Compd.*, 680 (2016). 694.
  18. Y. X. Lu, Y. Jiang, Z. Yang, J. T. Han, Y. H. Huang and J. Ma, *J. Alloys Compd.*, 559 (2013) 203.
  19. Y. M. Chin, R. A. Osman and M. S. Idris, *Appl. Mech. Mater.*, 754 (2015) 1187.
  20. Z. Li, C. Luo, C. Wang, G. Jiang, J. Chen, S. Zhong, Q. Zhang and D. Li, *J. Solid State Electrochem.*, 22 (2018) 2811.
  21. N. Murali, S. J. Margarete, J. M. Sailaja, V. K. Rao, P. Himakar, B. K. Babu and V. Veeraiah, *Mater. Sci. Eng.*, 310 (2018) 012126.
  22. S. T. Myung, S. Komaba, N. Hirosaki, K. Hosoya and N. Kumagai, *J. Power Sources*, 146 (2005) 645.
  23. S. Ko, S. C. Lee, C. W. Lee and J. S. Im, *J. Alloys Compd.*, 613 (2014) 96.
  24. Y. S. Lee, W. K. Shin, A. G. Kannan, S. M. Koo and D. W. Kim, *ACS Appl. Mater. Interfaces*, 7 (2015) 13944.
  25. Z. Lu, Z. Chen and J. R. Dahn, *Chem. Mater.*, 15 (2003) 3214.
  26. Y. Hinuma, Y. S. Meng, K. Kang and G. Ceder, *Chem. Mater.*, 19 (2007) 1790.
  27. J. Choi, S. Lee, S. Yoon, K. H. Kim, M. Kim, S. H. Hong, *ChemSusChem*, 7 (2019) 2439-2446.
  28. Y. Duan, L. Yang, M. J. Zhang, Z. Chen, J. Bai, K. Amine, F. Pan, F. Wang, *J. Mater. Chem. A*, 7 (2019) 513-519.